Role of the boundary layer dynamics effects on an extreme air pollution event in Paris

J. Dupont, M. Haeffelin, Jordi Badosa, T. Elias, O. Favez, J. Petit, F. Meleux, J. Sciare, V. Crenn, J.L. Bonne

Role of the boundary layer dynamics effects on an extreme air pollution event in Paris

J.-C. Dupont[(1)], M. Haeffelin[(1)], J. Badosa[(2)], T. Elias[(3)], O. Favez[(4)], JE. Petit[(4,5)*], F. Meleux[(4)], J. Sciare[(5)**], V. Crenn [(5)***], JL. Bonne[(5)]

(1) IPSL, Palaiseau, France ; (2) LMD, Palaiseau, France ; (3) HYGEOS, Lille, France ; (4) INERIS, Verneuil-en-Halatte, France; (5) LSCE, Gif-sur-Yvette, France

[*] *now at Air Lorraine, Metz, France*

[**] *now at the Cyprus Institute, Energy Environment Water Research Center, Nicosia, Cyprus*

[***] *now at ADDAIR, Buc, France*

Abstract.

[1] The physical and chemical aerosol properties are explored here based on ground-based observations in the Paris region to better understand the role of clouds, radiative fluxes and dynamics on aerosol loading during a heavy regional air pollution that occurred in March 2014 over North-Western Europe. This event is primarily characterized by a fine particle mass ($PM_{2.5}$) increase from 10 to more than 120 µg m^{-3} and a simultaneous decrease of the horizontal visibility from 40 to 1 km, mainly due to significant formation of ammonium nitrate particles. The aerosol optical depth (AOD) at 550 nm increased steadily from about 0.06 on March 6 to more than 0.9 five days later. The scattering of the solar radiation by polluted particles induced, at the peak of the heavy pollution event, an instantaneous shortwave flux decrease of about 300 W m^{-2} for direct irradiance and an increase of about 150 W m^{-2} for diffuse irradiance (only scattering). The mean surface aerosol effect efficiency (effect per unit optical depth) is of about -80 W m^{-2} with a mean aerosol direct radiative effect of -23 W m^{-2}. The dynamical and radiative processes that can be responsible for the diurnal cycle of $PM_{2.5}$ in terms of amplitude and timing are investigated. A comparative analysis is performed for 4 consecutive days (between March 11 and 14), showing that the $PM_{2.5}$ diurnal cycle can be modulated in time and amplitude by local processes such as the boundary layer depth development (ranging from 100 m to 1350 m), surface relative humidity (100 % to 35 %), thermal structure (10 °C to 16 °C for day/night amplitude), dynamics (wind speed ranging from 4 m s^{-1} to 1.5 m s^{-1}) and turbulence (turbulent kinetic energy reaching 2 m^2 s^{-2}) near the surface and wind shear along the vertical. Finally, modeled and measured surface $PM_{2.5}$ loadings are also compared here, notably illustrating the need of accurate boundary layer depth data for efficient air quality forecasts.

Introduction

[2] Aerosols significantly impact the global radiative energy balance of the Earth through scattering and absorption mechanisms of the solar irradiance, [Ramanathan et al., 2001]. In particular, the so-called aerosol direct radiative effect leads to *(i)* a cooling of the Earth's surface by scattering the solar radiation [Trenberth et al., 2009] but also to *(ii)* a warming of the atmosphere by absorbing the solar radiation [Wang et al., 2009]. At regional scale, the cooling effect due to anthropogenic aerosols may also be larger in magnitude than the greenhouse gas heating effect [Intergovernmental Panel on Climate Change (IPCC), 2015] and leads to complex climate feedback interactions [Shindell and Faluvegi, 2009]. Such effects of tropospheric aerosols depend on their physical properties [Wang et al., 2009; Barbaro et al., 2014], chemical composition [Yu and Zhang, 2011] and vertical distribution [Raut and Chazette, 2008]. Furthermore, aerosols can modify the vertical profile of temperature in the atmosphere [Barbaro et al., 2013] and the height of the boundary layer [Yu et al., 2002], and thus

affecting local weather patterns such as during the heat wave of summer 2003 over Western Europe [Pere et al., 2011].

[3] As recurrently observed in recent years during spring, a severe anthropogenic pollution event occurred over Paris and its surroundings in March 2014. The main objectives of the present study are to *(i)* characterize the aerosol properties, *(ii)* quantify the related direct radiative forcing as well as the mean surface aerosol effect on solar irradiance, and *(iii)* describe the role of dynamical, radiative and cloud processes on the particle mass variability over the Paris area during this pollution episode. To do so, the surface aerosol load and the physical processes have been investigated using in-situ, active and passive remote sensing.

Observational data set and modelling

Meteorological measurement: in-situ, active and passive instruments

[4] This study uses a dataset provided by the SIRTA observatory [Site Instrumental de Recherche par Télédétection Atmosphérique; Haeffelin et al., 2005], located 25 km south of Paris, France. SIRTA gathers active and passive remote sensing instruments, and is considered as representative of background air pollution in the Paris area [Petit et al., 2015]. High-quality shortwave and longwave irradiances are collected by a Baseline Surface Radiation Network station with 1-2% uncertainty [Ohmura et al., 1998]. Vertical distribution of particles (clouds and aerosols) in the 0-6 km is documented with a CL31 ceilometer leading to the determination of the Boundary Layer Depth (BLD) with STRAT+ algorithm [Morille et al., 2007; Haeffelin et al., 2012; Pal et al., 2013]. A Degreane DF20+ diffusometer is operated at 3 m above ground level (agl). A 6-stage, 30-m instrumented mast, equipped with temperature and humidity sensors, is extended vertically with radiosonde profiles (MODEM M10 sensor) that are performed routinely at 00:00 and 12:00 UTC, 15 km West of SIRTA as part of the Météo-France national network. A Leosphere WLS70 wind profiler Doppler lidar installed at SIRTA since March 2012 has been measuring the vertical profile of 3D wind components between 100 m and around 1500 m agl with a vertical resolution of 50 m. To complement the dynamics measurement near the ground level, we use a 3D sonic anemometer at 10 m agl to derive turbulent kinetic energy (noted here TKE in $m^2\ s^{-2}$) and sensible heat flux (noted H in $W\ m^{-2}$).

Aerosol measurement: in-situ and passive instruments

[5] A Cimel sun-photometer (multi-channel and automatic sun and sky scanning radiometer) from Aerosol Robotic Network (AERONET, Holben et al., 1998) is used to derive the Aerosol Optical Depth (AOD_{500}, here at 500 nm) and the Angstrom coefficient ($\alpha_{440\text{-}870}$, here between 440 and 870 nm). Level 2.0 data quality products are used here, allowing for the elimination of possible artifacts due to cloud detection and/or strong variability in aerosol loadings

$PM_{2.5}$ loadings (i.e., mass concentration of particle smaller than 2.5 µm) over the Paris area are calculated as the average value of TEOM-FDMS (Tapered Element Oscillating Microbalance – Filter Dynamics Measurement System, [Grover et al., 2005]) measurements performed by the regional air quality monitoring network (www.airparif.asso.fr) at three urban background stations (Gennevilliers, Bobigny and Vitry) around Paris.

The thorough in-situ characterization of the physical and chemical surface aerosol properties is performed at SIRTA – zone 5 (i.e., 4.5 km away from the main SIRTA platform). A TSI Scanning Mobility Particle Sizer (SMPS) allows for the measurement of dry aerosol size distribution between 10.6 and 496 nm. A multi-wavelength Aethalometer (AE33, Magee Scientific, Berkeley, CA, Drinovek

et al., 2014) measures the concentration of Black Carbon (BC). Finally, an Aerosol Chemical Speciation Monitor instrument (ACSM, Aerodyne, Billerica, MA, Ng et al., 2011) provides the concentrations of major non-refractory (NR) chemical components of dry aerosols (organic, ammonium, sulphate, nitrate and chloride) in the PM_1 fraction (i.e. aerodynamic diameter below 1 µm). This instrument has been continuously operating at SIRTA since mid-2011, with good correlations with other collocated automatic analysers as well as filter samples [Petit et al, 2015; Crenn et al., 2016].

Numerical simulations with PREV'AIR

[6] Modeling data are derived from numerical simulations on the PREV'AIR operational system [Rouil et al, 2009] dedicated to deliver daily forecast for the current day and up to two days ahead for a set of regulatory pollutants such as ozone, nitrogen dioxide and particulate matter (PM_{10} and $PM_{2.5}$). This air quality forecast is based on the chemical transport model CHIMERE [Menut et al, 2013] running over France at 10 x 10 km² and fed with GFS meteorological conditions provided by NCEP and the MACCII emission inventory [Kuenen et al, 2014] at 7 x 7 km^2. The chemical boundary conditions are provided using CHIMERE forecast over a coarser European domain. The boundary layer height is considered as the maximum of the boundary layer height calculated from the Richardson number profile [Troen and Mahrt, 1986], as the lowest altitude where Ri = 0.5, and a convectively based boundary layer height calculation [Rouil et al., 2009; Menut et al., 2013]. CHIMERE contains a sectional aerosol module which includes emitted total primary particulate matter (TPPM), secondary inorganic aerosols such as nitrate, sulphate, ammonium, and secondary organic aerosol. Boundary layer depth and $PM_{2.5}$ are simulated here for three Airparif urban background stations around the SIRTA Observatory: Gennevilliers, Bobigny and Vitry-sur-Seine.

Overview of observation and model output

[7] Figure 1A presents time-series of un-calibrated range-corrected attenuated backscatter profiles of CL31 ceilometer along with the Boundary Layer Depth (BLD) as derived from the STRAT+ algorithm (which makes use of backscatter and surface parameters, as described by Pal et al., 2013) and as modeled by PREV'AIR between March 09 and March 14. A nocturnal and stable BLD of about 100 m is obtained for the studied period, contrasting with much higher diurnal convective BLD ranging from 700 m for March 11 to 1400 m for March 13 and 14. A low-level cloud, based at 300 m, appeared on March 11 morning, whereas a fog event occurred on March 14 at 06:00 UT.

Figure 1B presents the time-series of the dry aerosol size distribution as well as measured and modeled $PM_{2.5}$ loadings, the latter ones notably increasing from 10 µg m^{-3} on March 09 to 125 µg m^{-3} on March 14 (10 to 200 µg m^{-3} for model). Figure 1C and 1D shows vertical profiles of wind speed and direction from WLS70 Doppler lidar respectively, as well as potential temperature and specific humidity profile from M10 radiosondes at 00:00 and 12:00. Results presented in these figures are further discussed in the following sections.

Aerosol properties and variability

Concentration, and chemical composition

[8] Figure 2 shows the submicron particle composition obtained from ACSM and Aethalometer measurements from February 28th to March 24th. This temporal window is divided into 4 distinct periods, for which the average chemical composition and PM_1 concentrations, and air masses backward trajectories are available. The latter are simulated using the Lagrangian atmospheric dispersion model Flexpart 8.2.3 (where 64 particles are released each hour from a box surrounding SIRTA and from 160 to 500 m above sea level, and transported 8 days backward). Periods I and III are

dominated by Westerly winds and oceanic air masses, which are predominant all along the year at SIRTA [Haeffelin et al., 2005; Petit et al., 2015]. These periods are associated with a high relative contribution of carbonaceous aerosols, OM and BC representing together more than 50 % of the fine aerosols, notably due to local combustion emissions [Petit et al., 2014]. Conversely, period II is primarily characterized by anticyclonic conditions, moderate wind speeds (ranging from 1 to 4 m s^{-1}) and an increase of the relative contributions of highly hygroscopic secondary inorganic aerosols (ammonium nitrate and ammonium sulfate). By contrast with periods I/III, fine aerosols in periods II may have a strong capacity to absorb water and increase their impact on light scattering as discussed later on in the present paper. This episode can be divided into 2 sub-periods, the first one (period IIa, from March 4th to March 9th) being dominated by a Northerly wind air mass, while the second one (period IIb, March 9th to 15th) mainly corresponds to Easterly wind and continental air masses, and is associated with highest PM_1 levels (up to 110 µg m^3 of PM_1). This pollution event is overwhelmingly composed of ammonium nitrate, a feature that is commonly observed during this period of the year in the Paris area [Sciare et al., 2010; Bressi et al., 2013; Petit et al., 2015], and more generally in North-Eastern Europe [Mooibroek et al., 2001; Waked et al., 2014]. Such high ammonium nitrate concentrations (up to 75 µg m^3 during the evening of March 14th) are related to favorable condensation of gaseous precursors (i.e., NO_X and NH_3, mainly originating from road transport and agricultural activities, respectively) in the particulate phase under high pressure systems combined with rather low temperature and/or high relative humidity conditions [Pay et al., 2012; Petetin et al., 2014]. These secondary inorganic aerosols species are produced through photochemical processes and partly formed in-situ (diurnal cycle in phase with solar radiation).

Optical properties and mass

Next we describe the sun-photometer AERONET data and the surface in-situ variables derived from the diffusometer and the TEOM-FDMS measurements. Figure 3 shows time-series of diurnal cycle of aerosol optical depth at 500 nm, Angstrom coefficient at 440/870 nm (B) horizontal visibility (C), particle mass $PM_{2.5}$ (D), between March 9 and March 14 2014. On March 9 2014 the average AOD is 0.08 to reach an average value of 0.7 on March 14 2014, indicating a continuous increase of the aerosol load in the total column of the atmosphere. During this period, the thin particle mode (particle radius ranging between 0.05 and 0.6 µm) dominate with an Angstrom coefficient larger than 1.3 except for March 11 characterized with specific conditions of humidity leading to aerosol growth (see below). Surface visibility at noon drops from 30 to 5 km whereas $PM_{2.5}$ increases from 30 to 110 µg m^3.

Aerosol radiative effect

[9] Figure 4 presents time-series of diurnal cycle of diffuse solar downwelling flux (A), direct solar downwelling flux (B) between March 9 and March 14 2014, respectively. Figures (4C) and (4D) show the relationship between column-integrated aerosol optical depth at 500 nm and surface-level extinction at 550 nmdepending on relative humidity (4C) and boundary layer depth (4D). Figure (4E) shows the relationship between column-integrated aerosol optical depth at 500 nm and Aerosol Direct Radiative Effect (ADRE) for direct, diffuse, and global irradiances.

[10] The ADRE for global shortwave irradiance [Heald et al., 2014], diffuse shortwave irradiance, direct shortwave irradiance and ultraviolet irradiance is defined as the difference between measured irradiance and the pristine clear-sky irradiance values that should be observed when the aerosol load is minimum [Dupont et al., 2009]. To quantify the ADRE, we use here the reference clear-sky pristine day of March 09 characterized by daily average AOD of about 0.08 at 550 nm and the maximum daily horizontal visibility of 22 km. The maximum radiative effect on diffuse downwelling flux is around +

150 W m^{-2} and -300 W m^{-2} for direct downwelling flux. The mean surface aerosol effect efficiency (effect per unit optical depth) is of about -80 W m^{-2}, +170 W m^{-2} and -600 W m^{-2} for global, diffuse and direct downwelling fluxes, respectively. The correlation coefficients are respectively 0.97, 0.90 and 0.91 (Figure 4E). Note that the instantaneous effects of aerosols on surface irradiance heavily depend on the solar zenith angle. In order to isolate the dependence of surface irradiance on the AOD value, the diurnal mean aerosol effect is computed to better represent the aerosol climatic effects. The diurnal mean aerosol effect efficiency is of about -72 W m^{-2}, +182 W m^{-2} and -604 W m^{-2} for global, diffuse and direct downwelling fluxes respectively, with very satisfactory correlation coefficients of 0.98, 0.94 and 0.95. These results are similar to the ones previously obtained by Liu et al. (2007). The average ADRF during the high-level pollution event is of -23 W m^{-2} for the downwelling shortwave global irradiance at the surface.

[11] For the ultraviolet radiative effect, UV measurements were corrected to remove the effect of the total ozone column levels (TOZ). Daily TOZ values were considered from Ozone Monitoring Instrument (OMI), and showed changes over SIRTA Observatory ranging from 295 to 349 DU during this period. The correction factor is developed based on clear-sky UV calculations for the whole period with the parametric PTUV model [Badosa et al, 2005]. The mean surface aerosol effect efficiency for UV irradiance at the surface is of about -0.7 W m^{-2} with a correlation coefficient around 0.92. The mean ultraviolet ARDF is of -0.35 W m^{-2}.

[12] Following Elias et al. (2010), we derived the Particle Extinction Coefficient (PEC) at 550 nm from horizontal visibility measurement at the surface, and we quantified the impact of relative humidity and boundary layer depth on the relationship between AOD and PEC (Figures 4C and 4D). We show the role of humidity on the aerosol growth (aerosol growth affects both AOT and PEC): the higher the RH for a same AOD, the larger the aerosol, due to the hygroscopicity factor leading to a decreasing in the visibility and so an increasing in the PEC. For example in Figure 4C, for AOD=0.2 and RH=50 %, PEC=80 M m^{-1}; whereas for AOD=0.2 and RH=85 %, PEC=450 M m^{-1}. In this situation, the Boundary Layer Depth plays a significant role to maintain a constant AOD whereas surface PEC is multiplied by 5. At RH=90 %, the size of ambient aerosol is larger due to hydration process and then contribute more efficiently to the extinction of visible radiation. The impact of Boundary Layer Depth on the relationship between AOD (integrated along the column) and PEC (local measurement at the surface) is significant and, as can be observed on Figure 4D, that for AOD=0.2 and BLD=800 m, PEC=70 M m^{-1} whereas for AOD=0.2 and BLD=150 m, PEC=300 M m^{-1}. For a higher BLD and a similar AOD, the aerosols are less homogeneously distributed along the vertical, so that the concentration near the surface is lower, leading to a smaller extinction of the visible radiation at the surface.

Physical processes driving the aerosol concentration at the surface level

[13] In this Section, we discuss the physical processes affecting the extreme pollution event, trying to establish a link between surface aerosol loading and chemical composition, radiative transfer, surface energy partitioning and boundary layer dynamics. The diurnal cycle of the BLD (Fig. 5A), surface radiative budget (Fig. 5B), turbulent kinetic energy (Fig. 5C), wind speed at 10m agl (Fig. 5D), vertical gradient of temperature (30m-1m, Fig. 5E), and sensible heat flux at 10m agl (Fig. 5F) are shown in Figure 5 for the period ranging between March 9 and March 14. The boundary layer depth is a signature of the intensity of the vertical mixing between the surface and the free troposphere. The vertical gradient of temperature between 30 and 1 m (T30-T1) provides the intensity of thermal stability. For example, on March 10 at 06:00 the thermal inversion between 1 and 30 m reaches 8 °C while the BLD remains very shallow around 70 m.

[14] During this 6-day period, we observe significant contrasts during each diurnal cycle of $PM_{2.5}$. As shown in Fig. (3D), $PM_{2.5}$ is modulated in time and in amplitude and we will quantify the role of dynamical, radiative, thermo-hygrometric and cloud processes on this variability. To do so, we analyzed precisely 4 days (March 11 to March 14) characterized by similar values of $PM_{2.5}$ at 08:00 UT near 90 µg m^{-3}. We identify four significant features characterizing the $PM_{2.5}$ diurnal cycle: (1) timing and intensity of the morning $PM_{2.5}$ maximum value, (2) timing and intensity of the afternoon $PM_{2.5}$ minimum value, (3) amplitude of the $PM_{2.5}$ cycle, and (4) $PM_{2.5}$ peak on evening of March 14.

[15] ***Timing and intensity of the morning $PM_{2.5}$ maximum value.*** $PM_{2.5}$ values at 08:00 UT are remarkably similar on all four days (March 11-14) near 90 µg m^{-3}, while $PM_{2.5}$ values are significantly difference from one day to the next, 3 hours later (70 µg m^{-3} on March 11 and 110 µg m^{-3} on March 14). The daily maximum $PM_{2.5}$ is reached at 09:00 UT on March 11 and March 12 (95 µg m^{-3} and 85 µg m^{-3}, respectively), whereas the maximum $PM_{2.5}$ is reached at 11:00 UT on March 13 and March 14 (near 110 µg m^{-3}). This two-hour difference can be related to the boundary layer depth development with a boundary layer starting to rise at 08:00 UT on March 11 and 12 against at 10:00 UT and 12:00 UT on March 13 and March 14 respectively. On March 11, the $PM_{2.5}$ decrease is quite limited (-3 µg m^{-3} per hour) whereas it reaches -7 µg m^{-3} per hour on March 12. This significant contrast should be related to the thickness of aerosol dilution characterized here by the boundary layer growth rate around 50 m hr^{-1} on March 11 and 150 m hr^{-1} on March 12 (typical of winter-time growth rates according to Pal and Haeffelin, 2015). On March 13 and 14, the $PM_{2.5}$ decrease starting from the maximum at 11:00 UT is of about -7 µg m^{-3} per hour for a boundary layer growth rate larger than +300 m hr^{-1} (typical of summer-time values). However, the $PM_{2.5}$ temporal difference of one hour between March 13 and 14 can be explained by a more rapid decrease on March 13 in relation with the fastest development of the BLD (1000 m at 12:00 on March 13 and 500 m at 12:00 on March 14). The delay for the boundary layer depth development concerning March 14 is likely due to fog formation at 06:00 and dissipation at 07:30. The dissipation of the fog layer delays the thermal eddies and so the vertical mixing. Consequently, temporal evolution between 06:00 and 09:00 is drastically different on March 13 and March 14. The 2m-temperature temporal gradient is around +3 °C h^{-1} against +2 °C h^{-1}, and decreasing relative humidity from 90 % to 60 % against saturated air mass with 100 % relative humidity value. Moreover, the BLD development on March 14 could also be affected by the vertical profile of wind shear (Fig. 1D) that tends to modify air mass origin and then aerosol, temperature and humidity profiles (Fig. 1A, 1C and 1D).

[16] ***Timing and intensity of the afternoon $PM_{2.5}$ minimum value.*** Minimum value of $PM_{2.5}$ occurs in the afternoon but we note major differences within the March 11 – March 14 period. The minimum value of $PM_{2.5}$ is 75 µg m^{-3} and occurs at 15:00 UT on March 11 and at 18:00 UT on the three other days, with 45 µg m^{-3}, 55 µg m^{-3} and 60 µg m^{-3} on March 12, March 13 and March 14 respectively. Hence, March 11 is characterized by the highest afternoon polluted aerosol concentration whereas the aerosol optical depth is quite limited at 0.4 against higher than 0.7 on March 13 and March 14. Simultaneously, horizontal visibility equals to 6 km, 8 km and 9 km respectively on March 11, March 13 and March 14. The afternoon aerosol concentration near the ground level can be correlated with the boundary layer depth (layer of dilution for aerosols and mixing): 700 m for March 11, and 1200 m for March 13 and March 14. The stronger wind speed between surface and 1 km on March 11, reaching more than 15 m s^{-1} at 500 m, can explain the limited development of the boundary layer on that day (Fig. 1C). By contrast, March 13 and 14 are much less turbulent with maximum wind speed around 6 m s^{-1}. The vertical development of the boundary layer on March 13 and 14 is driven by the solar heating leading to thermal eddies, while the important wind shear on March 11 tends to limit these thermal eddies and so the vertical mixing. The top of the boundary layer corresponds to the altitude where the wind shear is at its maximum, which occurs near 700 m on March 11. This thin

BLD confines the humidity near the surface and can explain the very high value of relative humidity larger than 60% during daytime compared to the another days (smaller than 40 % and 30 % on March 13 and March 14). The strong mixing between surface and some hundreds of meter on March 11 (at the opposite, low mixing for March 13 and 14) characterized by 10-m TKE and 10-m wind speed larger than 3 m^2 s^{-2} and 4 m s^{-1}, respectively, (smaller than 0.3 m^2 s^{-2} and 1 m s^{-1}, Fig. 5C and Fig. 5D), tends to homogenize temperature (Fig. 1C) and humidity (Fig. 1D) profiles in the boundary layer. On March 11, the vertical profile of specific humidity and potential temperature are constant until 400 m at 00:00 and 500 m at 12:00. The upper air parcel is drier but vertical wind speed is very small (smaller than -0.2 m s^{-1} during nighttime period), limiting considerably the entrainment of dry air originating from the residual layer or free troposphere. Consequently, the wetter boundary layer on March 11 persists during all the day.

[17] ***Amplitude of $PM_{2.5}$ cycle.*** $PM_{2.5}$ daytime variations on March 11 are very limited with a maximum of 90 µg m^{-3} at 06:00 and a minimum of 70 µg m^{-3} at 18:00 compared to March 14 with 110 µg m^{-3} at 11:00 and 55 µg m^{-3} at 18:00. On March 11, BLD ranged from 300 m to 650 m against 150m to 1450m on March 14, leading to a daytime dilution effect more than twice smaller on March 11. The relative humidity ranges from 100 % to 60 % and from 80 % to 35 % on March 11 and March 14, respectively. We note major differences in day-night temperature amplitudes equal to 10°C on March 11 and 16°C on March 14. Moreover, the important mixing between the surface and the top of the boundary layer on March 11 (TKE higher than 1 m^2 s^{-2} and wind speed around 4 m s^{-1}) tends to homogenize the vertical profile of aerosol concentration and temperature/humidity (Fig. 1C and 1D). It drives the diurnal cycle of $PM_{2.5}$ with low concentrations before 12:00 (for a BLD larger than on other days) and highest loadings around 15:00-18:00 (for a BLD shallower than on other days). Moreover, on March 13 $PM_{2.5}$ variations follow the AOD, while on March 14 $PM_{2.5}$ variations seem to be anti-correlated with the AOD. The BLD is quite similar on March 13 and March 14, in spite of inhomogeneous aerosol vertical profiles. Consequently, the relationship between AOD and $PM_{2.5}$ is more complex on March 14 and a phenomenon such as the one described by Curci et al. (2015) is a possible explanation: the upper-level processes within and above the boundary layer can contribute up to 40% of the $PM_{2.5}$. The vertical profile of aerosol properties (size, concentration, composition) will be analyzed in a future work to better understand the relationship between aerosol, gas, and thermodynamical variables.

[18] ***$PM_{2.5}$ peak on evening of March 14.*** The maximum $PM_{2.5}$ (125 µg m^{-3}) observed during the 6-day period occurs on March 14 at 23:00 UT, when more than 70 % of the PM_1 fraction is made of NO_3 and NH_4. Nitrate and ammonium ions are known to be hydrophilic, enhancing the aerosol growth. On March 14 at 22:00 UT, particles larger than 100 nm are twice more important than on March 13 at the same time (approximately 1500 # cm^{-3} against 800 # cm^{-3} respectively), playing a major role in the $PM_{2.5}$ increase. After 23:00 UT, $PM_{2.5}$ starts decreasing, possibly due to the fog formation and the activation of fine particles into droplets larger than 2.5 µm in aerodynamic diameter. Typically, during a fog event droplet size distributions are centered on 20 µm with minimum and maximum size at 3µm and 50µm, respectively [Degefie et al., 2015]. A supersaturation around 0.03 % is favorable for the fog formation [Hammer et al., 2014] and this condition is reached on March 14 at 23:00.

[19] ***Difference between observed and modeled PM2.5***. The observed and modeled $PM_{2.5}$ time series are characterized by significant differences in timing and amplitude (Figure 1.A, 1.B). A possible reason to explain these discrepancies relies in the difference between modeled and measured boundary layer depths (dilution effect). Indeed, when modeled $PM_{2.5}$ is higher than observed $PM_{2.5}$ (March 10 at 09:00, March 13 at 09:00 and March 13 at 18:00), the modeled BLD is much lower than the observed BLD (20 m and 90 m on March 10 at 09:00, 20 m and 108 m on March 13 at 09:00, 60 m

and 110 m on March 13 at 18:00). By contrast, the modeled $PM_{2.5}$ is lower than observed $PM_{2.5}$ (March 9 during night, March 11 and 12 until 12:00) when the former one BLD is higher than latter one (270 m and 110 m on March 9 during night, relatively constant difference of 200 m between March 11and March 12 until 12:00). The transitions between cloud-free night (very stable thermal conditions) and clear-sky day (unstable thermal conditions) and vice versa induce strong variations of BLD and modulate significantly $PM_{2.5}$, leading to important differences during this specific period. However, the constant and significant difference during more than 36 hours (March 11 until March 12 18:00) between modeled $PM_{2.5}$ (mean value around 35 µg m^{-3}) and observed $PM_{2.5}$ (mean value around 80 µg m^{-3}) can be related to the cloud formation during the night and high relative humidity value in the whole day with a limited vertical development of the boundary layer.

Conclusions

[19] Surface-based observations gathered at SIRTA Observatory are used to identify the major mechanisms driving the heavy regional air pollution episode that affected the Paris region in March 2014, and to quantify the impacts of this particulate pollution on the surface visibility and on the solar and ultraviolet downwelling irradiances at the surface. $PM_{2.5}$, mainly composed of ammonium nitrate and organic matter, ranged from 10 to more than 120 µg m^{-3} during the studied period. Concomitantly, the aerosol optical depth at 550 nm increased steadily from about 0.06 on March 6 to more than 0.9 five days later with a horizontal visibility decreasing from 40 to less than 1 km. The absorption and scattering of solar radiation by pollution particles induced, at the peak of the heavy pollution event, a direct irradiance instantaneous shortwave flux decrease of about 450 W m^{-2} and a diffuse irradiance instantaneous shortwave flux increase of about 150 W m^{-2}. The mean aerosol direct radiative effect during this period was -23 W m^{-2} for shortwave and -0.35 W m^{-2} for ultraviolet irradiances. The mean surface aerosol effect efficiency (effect per unit optical depth) was of about -80 W m^{-2} and -0.7 W m^{-2} for shortwave and ultraviolet irradiances, respectively. We show with a comparative study that the vertical development of boundary layer can be inversely correlated to the diurnal cycle of $PM_{2.5}$, with variations that are consistent in time and amplitude. On March 14, $PM_{2.5}$ ranged from 110 µg m^{-3} at 11:00 (BLD = 150 m) to 55 µg m^{-3} at 18:00 (BLD = 1450 m), while on March 11 , $PM_{2.5}$ ranged from 90 µg m^{-3} at 06:00 (BLD = 300 m) and 70 µg m^{-3} at 18:00 (BLD = 650 m). The boundary layer depth is afected by solar heating of the surface, surface dynamics and turbulence but also by vertical wind shear. Hence, we are able to identify here the signature of the local dynamical processes (vertical mixing, boundary layer depth) on the particle mass near the ground level by comparing diurnal cycle obtained by observations. This methodology can be applied to other case studies in order to statistically investigate the various processes affecting particulate pollution episodes.

Acknowledgements

[19] The authors would like to thank the technical and computer staffs of SIRTA Observatory for taking the observations and making the data set easily accessible. The authors would like to acknowledge Météo-France for providing CL31 and radiosonde data, CEREA for providing WLS70 data, Airparif for providing PM2.5 data, AERONET for providing the AOD data. This work was partly funded by the ACTRIS program (European Union Seventh Framework Program (FP7/2007-2013), grant agreement n° 262254).

References

Barbaro, E., J. Vilà-Guerau de Arellano, M. C. Krol, and A. A. M. Holtslag (2013), Impacts of aerosol shortwave radiation absorption on the dynamics of an idealized convective atmospheric boundary layer, *Boundary Layer Meteorol.*, 148, 31–49, doi:10.1007/s10546-013-9800-7.

Barbaro, E., J. Vilà-Guerau de Arellano, H. G. Ouwersloot, J. S. Schröter, D. P. Donovan, and M. C. Krol (2014), Aerosols in the convective boundary layer: Shortwave radiation effects on the coupled land-atmosphere system, *J. Geophys. Res. Atmos.*, 119, doi:10.1002/2013JD021237.

Bessagnet, B., Hodzic, A., Blanchard, O., Lattuati, M., Le Bihan, O., Marfaing, H., Rouil, L., Origin of particulate matter pollution episodes in wintertime over the Paris Basin, *Atmos. Environ.*, 39, 6159-6175, 2005.

Bressi, M., Sciare, J., Ghersi, V., Bonnaire, N., Nicolas, J. B., Petit, J.-E., Moukhtar, S., Rosso, A., Mihalopoulos, N. and Féron, A.: A one-year comprehensive chemical characterisation of fine aerosol (PMF) at urban, suburban and rural background sites in the region of Paris (France), *Atmospheric Chem. Phys.*, 13(15), 7825–7844, doi:10.5194/acp-13-7825-2013, 2013.

Curci, G., Ferrero, L., Tuccella, P., Barnaba, F., Angelini, F., Bolzacchini, E., Carbone, C., Denier van der Gon, H. A. C., Facchini, M. C., Gobbi, G. P., Kuenen, J. P. P., Landi, T. C., Perrino, C., Perrone, M. G., Sangiorgi, G., and Stocchi, P.: How much is particulate matter near the ground influenced by upper-level processes within and above the PBL? A summertime case study in Milan (Italy) evidences the distinctive role of nitrate, *Atmos. Chem. Phys*., 15, 2629-2649, doi:10.5194/acp-15-2629-2015, 2015.

Drinovec, L., Mocnik, G., Zotter, P., Prevot, A. S. H., Ruckstuhl, C., Coz Diego, E., Rupakheti, M., Sciare, J., Mueller, T., Wiedensohler, A. T. and Hansen, A. D. A.: The "Dual-Spot" Aethalometer: improved measurement of Aerosol Black Carbon with real-time loading compensation, *Atmos Meas Tech Discuss*, 2014.

Elias T., Haeffelin M., Drobinski P., Gomes L., Rangognio J., Bergot T., Chazette P., Raut J.-C. and Colomb M. (2010), Particulate contribution to extinction of visible radiation: pollution, haze, and fog, Atm. Res., 92,443-454.

Heald, C. L., D. A. Ridley, J. H. Kroll, S. R. H. Barrett, K. E. Cady-Pereira, M. J. Alvarado, and C. D. Holmes (2014), Contrasting the direct radiative effect and direct radiative forcing of aerosols, *Atmos. Chem. Phys.*, 14, 5513-5527, doi:10.5194/acp-14-5513-2014,

Grover, B.D. (2005), Measurement of total $PM_{2.5}$ mass (nonvolatile plus semivolatile) with the Filter Dynamic Measurement System tapered element oscillating microbalance monitor, *J. Geophys. Res.*, 110(D7), doi:10.1029/2004JD004995, 2005.

Haeffelin M., L. Barthès, O. Bock, C. Boitel, S. Bony, D. Bouniol, H. Chepfer, M. Chiriaco, J. Cuesta, J. Delanoë, P. Drobinski, J.-L. Dufresne, C. Flamant, M. Grall, A. Hodzic, F. Hourdin, F. Lapouge, Y. Lemaître, A. Mathieu, Y. Morille, C. Naud, V. Noël, W. O'Hirok, J. Pelon, C. Pietras, A. Protat, B. Romand, G.Scialom, and R. Vautard (2005), SIRTA, a ground-based atmospheric observatory for cloud and aerosol research, *Annales Geophysicae*, *23*, 262-275

Haeffelin, M., F. Angelini, Y. Morille, G. Martucci, S. Frey, G.-P. Gobbi, S. Lolli, C. D. O'Dowd, L. Sauvage, I. Xueref-Rémy, B. Wastine, D. Feist (2012), Evaluation of mixing height retrievals from automatic profiling lidars and ceilometers in view of future integrated networks in Europe, Boundary-Layer Meteorol. 143:49–75.

Holben, B. N., and Coauthors, 1998: AERONET—A federated instrument network and data archive for aerosol characterization, *Remote Sens. Environ.*, 66, 1–16.

Kuenen, J. J. P. , A. J. H. Visschedijk, M. Jozwicka, and H. A. C. Denier van der Gon, TNO-MACC_II emission inventory; a multi-year (2003–2009) consistent high-resolution European emission inventory for air quality modelling, *Atmos. Chem. Phys.*, 14, 10963-10976, 2014

Liu J., X. Xia, P. Wang, Z. Li, Y. Zheng, M. Cribb, and H. Che, 2007 Significant aerosol direct radiative effects during a pollution episode in northern China, *Geophysical Research Letter*, vol. 34, L23808, doi:10.1029/2007GL030953

Menut L., B. Bessagnet, D. Khvorostyanov, M. Beekmann, N. Blond, A. Colette, I. Coll, G. Curci, G. Foret, A. Hodzic, S. Mailler, F. Meleux, J.L. Monge, I. Pison, G. Siour, S. Turquety, M. Valari, R. Vautard and M.G. Vivanco, 2013, CHIMERE 2013: a model for regional atmospheric composition modelling, *Geoscientific Model Development*, 6, 981-1028, doi:10.5194/gmd-6-981-2013

Mooibroek, D., Schaap, M., Weijers, E. P., and Hoogerbrugge, R.: Source apportionment and spatial variability of PM2.5 using measurements at five sites in the Netherlands, *Atmos. Environ.*, 45, 4180–4191, doi:10.1016/j.atmosenv.2011.05.017, 2011.

Morille Y., M. Haeffelin, P. Drobinski, J. Pelon (2007), STRAT: An Automated Algorithm to Retrieve the Vertical Structure of the Atmosphere from Single-Channel Lidar Data, *J. Atmos. Ocean. Technol.*, 24, 761–775.

Ng, N. L., S. C. Herndon, A. Trimborn, M. R. Canagaratna, P. L. Croteau, T. B. Onasch, D. Sueper, D. R. Worsnop, Q. Zhang, Y. L. Sun and J. T. Jayne, An Aerosol Chemical Speciation Monitor (ACSM) for Routine Monitoring of the Composition and Mass Concentrations of Ambient Aerosol (2011), *Aerosol Sci. Tech.*, 45, 770-784, DOI: 10.1080/02786826.2011.560211.

Ohmura, A., Dutton, E., Forgan, B., Fröhlich, C., Gilgen, H., Hegner, H., Heimo, A., König-Langlo, G., Müller, G., Philipona, R., Pinker, R., Whitlock, C., Dehne, K., and Wild, M. (1998), Baseline Surface Radiation Network (BSRN/WCRP): New Precision Radiometry for Climate Research, *Bulletin of the American Meteorological Society*, 79, 2115–2136

Pal, S., M. Haeffelin, and E. Batchvarova (2013), Exploring a geophysical process-based attribution technique for the determination of the atmospheric boundary layer depth using aerosol lidar and near-surface meteorological measurements, *J. Geophys. Res. Atmos.* , 118 , doi:10.1002/jgrd.50710

Pal, S., and M. Haeffelin (2015), Forcing mechanisms governing diurnal, seasonal, and interannual variability in the boundary layer depths: Five years of continuous lidar observations over a suburban site near Paris, J. Geophys. Res. Atmos., 120, 11,936–11,956, doi:10.1002/2015JD023268.

Pay, M. T., Jiménez-Guerrero, P. and Baldasano, J. M.: Assessing sensitivity regimes of secondary inorganic aerosol formation in Europe with the CALIOPE-EU modeling system, *Atmos. Environ.*, 51, 146–164, doi:10.1016/j.atmosenv.2012.01.027, 2012.

Péré, J. C., M. Mallet, V. Pont, and B. Bessagnet (2011), Impact of aerosol direct radiative forcing on the radiative budget, surface heat fluxes, and atmospheric dynamics during the heat wave of summer 2003 over Western Europe: A modeling study, *J. Geophys. Res.*, 116, D23119, doi:10.1029/2011JD016240.

Petetin, H., Beekmann, M., Sciare, J., Bressi, M., Rosso, A., Sanchez, O. and Ghersi, V.: A novel model evaluation approach focussing on local and advected contributions to urban PM2.5 levels –

application to Paris, France, Geosci. Model Dev. Discuss. 6(4), 6391–6457, doi:10.5194/gmdd-6-6391-2013, 2013.

Petit, J.-E., Favez, O., Sciare, J., Canonaco, F., Croteau, P., Močnik, G., Jayne, J., Worsnop, D. and Leoz-Garziandia, E.: Submicron aerosol source apportionment of wintertime pollution in Paris, France by Double Positive Matrix Factorization (PMF²) using Aerosol Chemical Speciation Monitor (ACSM) and multi-wavelength Aethalometer, *Atmospheric Chem. Phys.*, 14(10), 13773-13787, doi:10.5194/acp-14-13773-2014, 2014.

Petit, J.-E., Favez, O., Sciare, J., Crenn, V., Sarda-Estève, R., Bonnaire, N., Močnik, G., Dupont, J.-C., Haeffelin, M., and Leoz-Garziandia, E.: Two years of near real-time chemical composition of submicron aerosols in the region of Paris using an Aerosol Chemical Speciation Monitor (ACSM) and a multi-wavelength Aethalometer, *Atmos. Chem. Phys.*, 15, 2985-3005, doi:10.5194/acp-15-2985-2015, 2015

Ramanathan, V., P. J. Crutzen, J. T. Kiehl, and D. Rosenfeld (2001), Aerosols, climate, and the hydrological cycle, *Science*, 294, 2119–2124.Trenberth et al., 2009

Raut, J.-C., and P. Chazette (2008), Radiative budget in the presence of multi-layered aerosol structures in the framework of AMMA SOP-0, *Atmos. Chem. Phys. Discuss.*, 8(4), 12,461–12,528, doi:10.5194/acpd-8-12461-2008.

Rouil, L., C. Honoré, B. Bessagnet, L. Malherbe, F. Meleux, R. Vautard, M. Beekmann, J.-M. Flaud, A. Dufour, D. Martin, A. Peuch, V.-H. Peuch, C. Elichegaray, N. Poisson, and L. Menut, 2009: Prev'air: an operational forecasting and mapping system for air quality in europe. *Bull. Amer. Meteor. Soc.*, 90, 73–83, doi: http://dx.doi.org/10.1175/2008BAMS2390.14

Sciare, J., d' Argouges, O., Zhang, Q. J., Sarda-Estève, R., Gaimoz, C., Gros, V., Beekmann, M. and Sanchez, O.: Comparison between simulated and observed chemical composition of fine aerosols in Paris (France) during springtime: contribution of regional versus continental emissions, *Atmospheric Chem. Phys.*, 10(24), 11987–12004, doi:10.5194/acp-10-11987-2010, 2010.

Shindell, D., and G. Faluvegi (2009), Climate response to regional radiative forcing during the twentieth century, Nat. Geosci., 2, 294 – 300

Waked, A., Favez, O., Alleman, L. Y., Piot, C., Petit, J.-E., Delaunay, T., Verlinden, E., Golly, B., Besombes, J.-L., Jaffrezo, J.-L. and Leoz-Garziandia, E.: Source apportionment of PM10 in a north-western Europe regional urban background site (Lens, France) using positive matrix factorization and including primary biogenic emissions, Atmospheric Chem. Phys., 14(7), 3325–3346, doi:10.5194/acp-14-3325-2014, 2014.

Wang, Y., H. Che, J. Ma, Q. Wang, G. Shi, H. Chen, P. Goloub, and X. Hao (2009), Aerosol radiative forcing under clear, hazy, foggy, and dusty weather conditions over Beijing, China, Geophys. Res. Lett., 36, L06804, doi:10.1029/2009GL037181.

Wang, P., W. H. Knap, P. Kuipers Munneke, and P. Stammes (2009), Clear-sky shortwave radiative closure for the Cabauw Baseline Surface Radiation Network site, Netherlands, J. Geophys. Res., 114, D14206, doi:10.1029/2009JD011978.

Yu, H., S. C. Liu, and R. E. Dickinson (2002), Radiative effects of aerosols on the evolution of the atmospheric boundary layer, J. Geophys. Res., 107, D124142, doi:10.1029/2001JD000754.

Yu, S., and Y. Zhang (2011), An examination of the effects of aerosol chemical composition and size on radiative properties of multi-component aerosols, Atmos. Clim. Sci., 1(2), 19–32, doi:10.4236/acs.2011.12003.

Role of the boundary layer dynamics effects on an extreme air pollution event in Paris

J.-C. Dupont[(1)], M. Haeffelin[(1)], J. Badosa[(2)], T. Elias[(3)], O. Favez[(4)], JE. Petit[(4,5)*], F. Meleux[(4)], J. Sciare[(5)**], V. Crenn [(5)***], JL. Bonne[(5)]

(1) IPSL, Palaiseau, France ; (2) LMD, Palaiseau, France ; (3) HYGEOS, Lille, France ; (4) INERIS, Verneuil-en-Halatte, France; (5) LSCE, Gif-sur-Yvette, France

[*] *now at Air Lorraine, Metz, France*

[**] *now at the Cyprus Institute, Energy Environment Water Research Center, Nicosia, Cyprus*

[***] *now at ADDAIR, Buc, France*

TABLE

Instruments	Parameter	Temporal resolution	Uncertainty
CL31 Ceilometer Nd-YAG (910 nm)	Cloud base height [Morille at al., 2007] Boundary Layer Depth [Pal et al., 2013]	30 sec	15 m
Surface pyrgeometer and pyranometer	Shortwave and Longwave downwelling and upwelling fluxes (W m-2)	1 min	4 W m-2 for longwave 5 W m-2for shortwave
Degreanne DF20+ visibilimeter	Horizontal visibility (km)	1 min	± 10-25 %
Temperature and humidity sensors located at 1, 2, 5, 10 et 30 m agl	Temperature and humidity at 5 levels above the ground	1 min	0.2 °C for temperature 2 % for relative humidity
Cimel sun-photometer, level 1 products	Aerosol optical depth at 500nm Angstrom coefficient at 440/870nm	Around 10min when solar is visible	0.002-0.005
M10 Modem radiosondes	Pressure, temperature, humidity, wind speed and direction Altitude between 0 and 20 km)	00:00 and 12:00 UTC	0.2 °C for T 2 % for RH
Cup anemometer and wind vane	Wind speed and wind direction at 10m	1 min	$0.1 ms^{-1}$ and ±2°
CSAT-3 sonic anemometer	Turbulent heat flux Momentum flux	10Hz for raw data 5min for TKE and sensible heat flux	5-15%
WLS70 Doppler wind lidar	3D wind speed between 100m and 1500m	10min	0.1m/s and 2°
TSI SMPS	Dry aerosol number concentration and size distribution (10.6 to 496nm)	5min	10 %
ACSM	Aerosol chemistry (organic, ammonium, sulfate, nitrate and chloride)	30min	$0.2 \mu g m^{-3}$
TEOM -FDMS (tapered element oscillating microbalance)	PM2.5 mass concentration (µg m-3)	15 min	±1.5 µg m-3
AE33 Aethalometer	Black Carbon	1 min	20 %

Table 1. Active and passive remote sensing instruments and the in-situ sensors used for this study. All instruments are deployed at the SIRTA site, except for $PM_{2.5}$ TEOM-FDMS measurements provided by the regional air quality monitoring network (AIRPARIF) at different urban background stations of the Paris region.

Role of the boundary layer dynamics effects on an extreme air pollution event in Paris

J.-C. Dupont[(1)], M. Haeffelin[(1)], J. Badosa[(2)], T. Elias[(3)], O. Favez[(4)], JE. Petit[(4,5)*], F. Meleux[(4)], J. Sciare[(5)**], V. Crenn [(5)***], JL. Bonne[(5)]

(1) IPSL, Palaiseau, France ; (2) LMD, Palaiseau, France ; (3) HYGEOS, Lille, France ; (4) INERIS, Verneuil-en-Halatte, France; (5) LSCE, Gif-sur-Yvette, France

[*] *now at Air Lorraine, Metz, France*

[**] *now at the Cyprus Institute, Energy Environment Water Research Center, Nicosia, Cyprus*

[***] *now at ADDAIR, Buc, France*

FIGURES

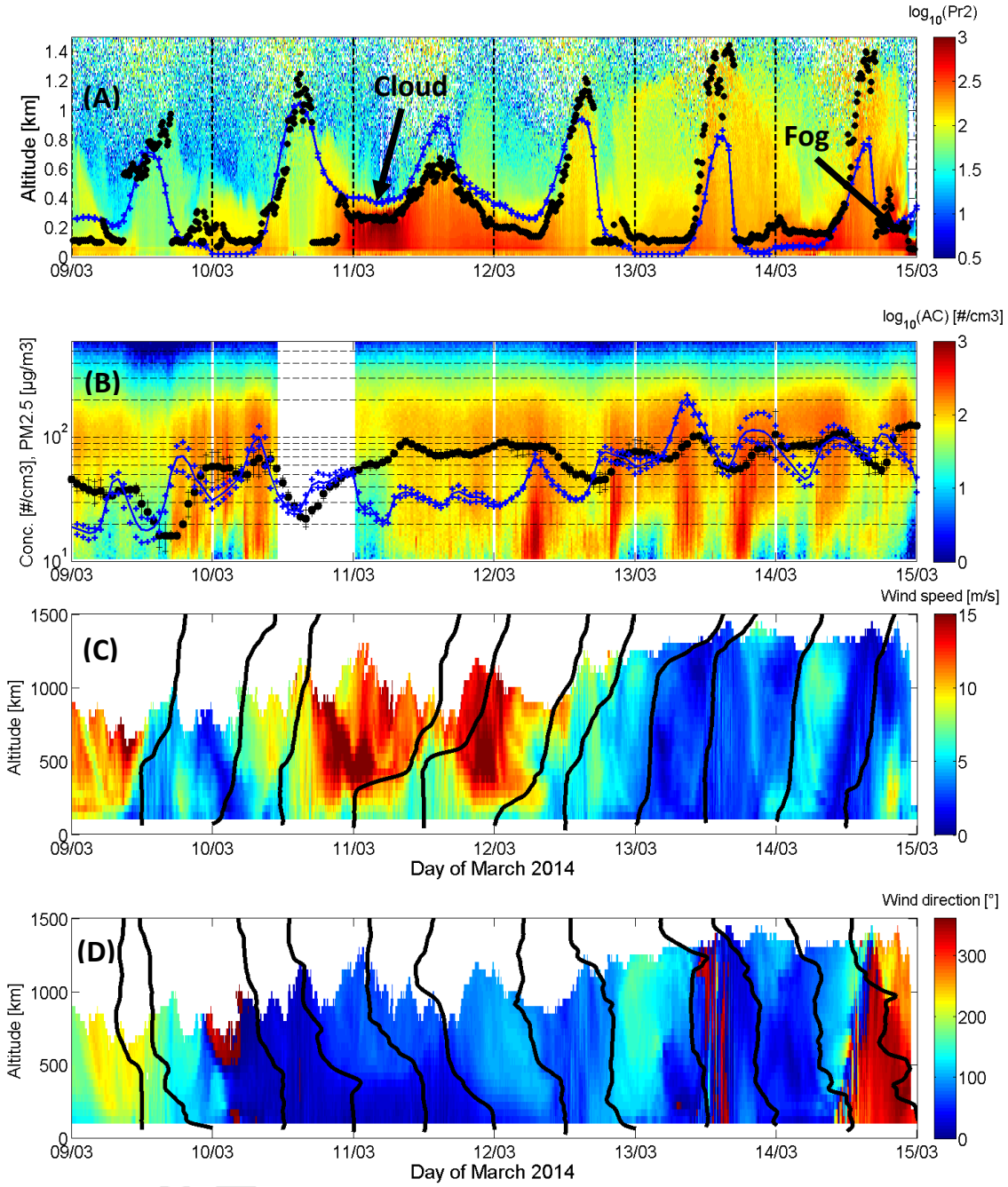

Figure 1. Time series of (Fig. 1A) attenuated backscatter signal (color bar) and boundary layer depth derived from CL31 ceilometer (black line) or modelled (blue line : average value of the Gennevilliers, Bobigny and Vitry, and blue square markers : max and min values of the three sites); (Fig. 1B) aerosol size distribution from TSI SMPS (color bar) and PM2.5 from TEOM FDMS (black marker) or from model (blue line : average value of the Gennevilliers, Bobigny and Vitry, and blue square markers : max and min values of the three sites); (Fig. 1C) vertical profile of wind speed from WLS70 Doppler lidar (color bar) and potential temperature profile from M10 radiosondes (black line) ; (Fig. 1D) vertical profile of wind direction from WLS70 Doppler lidar (color bar) and specific humidity profile from M10 radiosondes (black line).

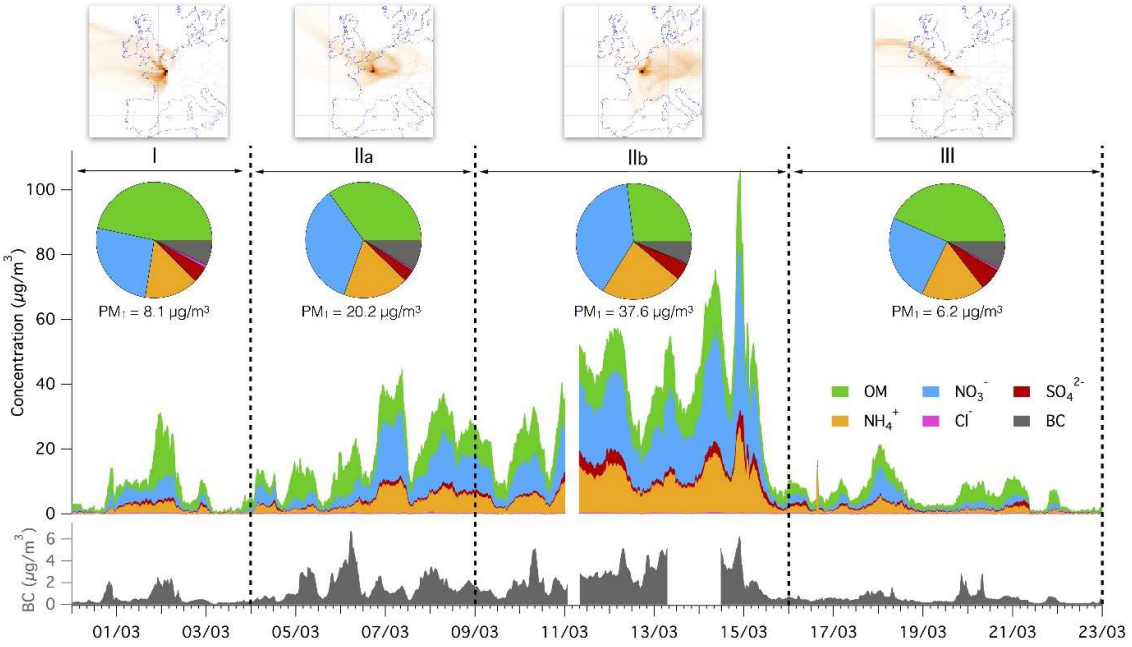

Figure 2. Temporal variations of the chemical composition of submicron aerosols from ACSM and Aethalometer measurements before, during and after the high level pollution event. The top panel shows the average Flexpart backtrajectories for each delimited period, represented as the number of particles crossing each 0.5°x0.5° grid cell during the 8 days of transport, relatively to the maximum of this number over the grid.

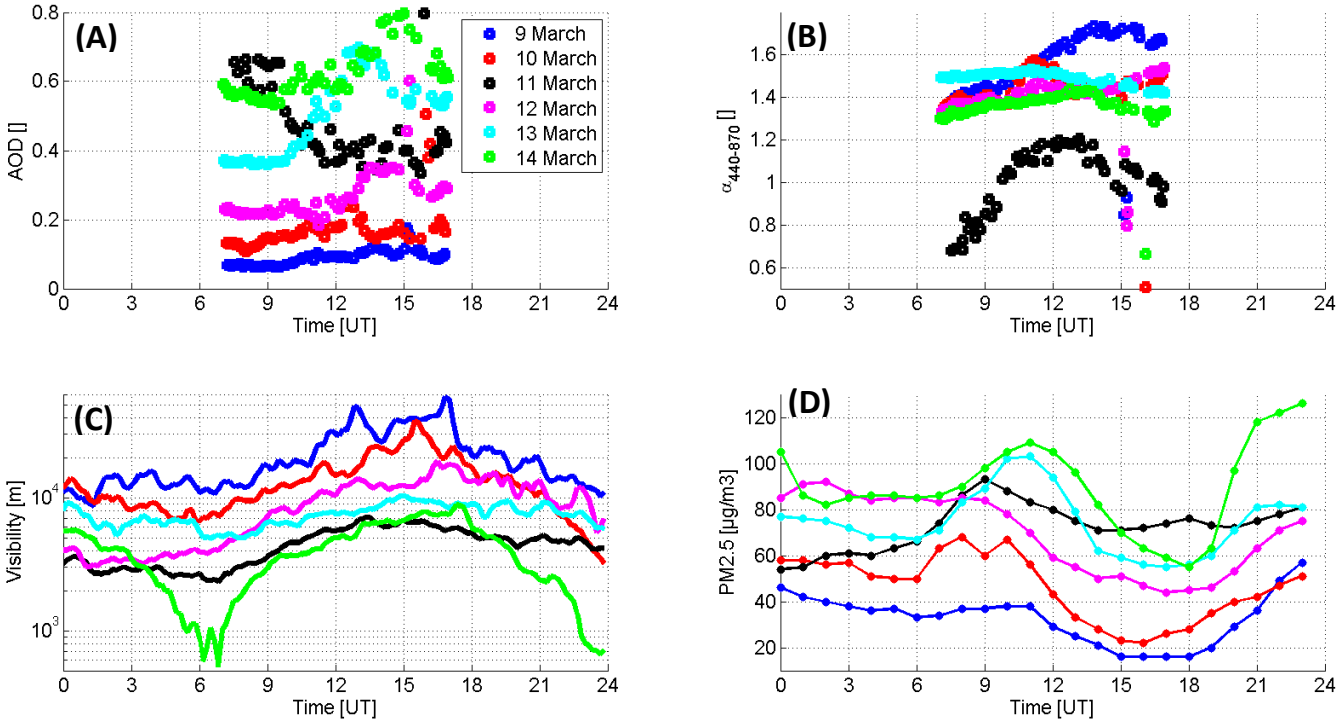

Figure 3. Diurnal cycle of aerosol optical depth at 500nm (Fig. 3A), Angstrom coefficient at 440/870nm (Fig. 3B) horizontal visibility (Fig. 3C), particle mass PM2.5 (Fig. 3D), between March 9 and March 14 2014.

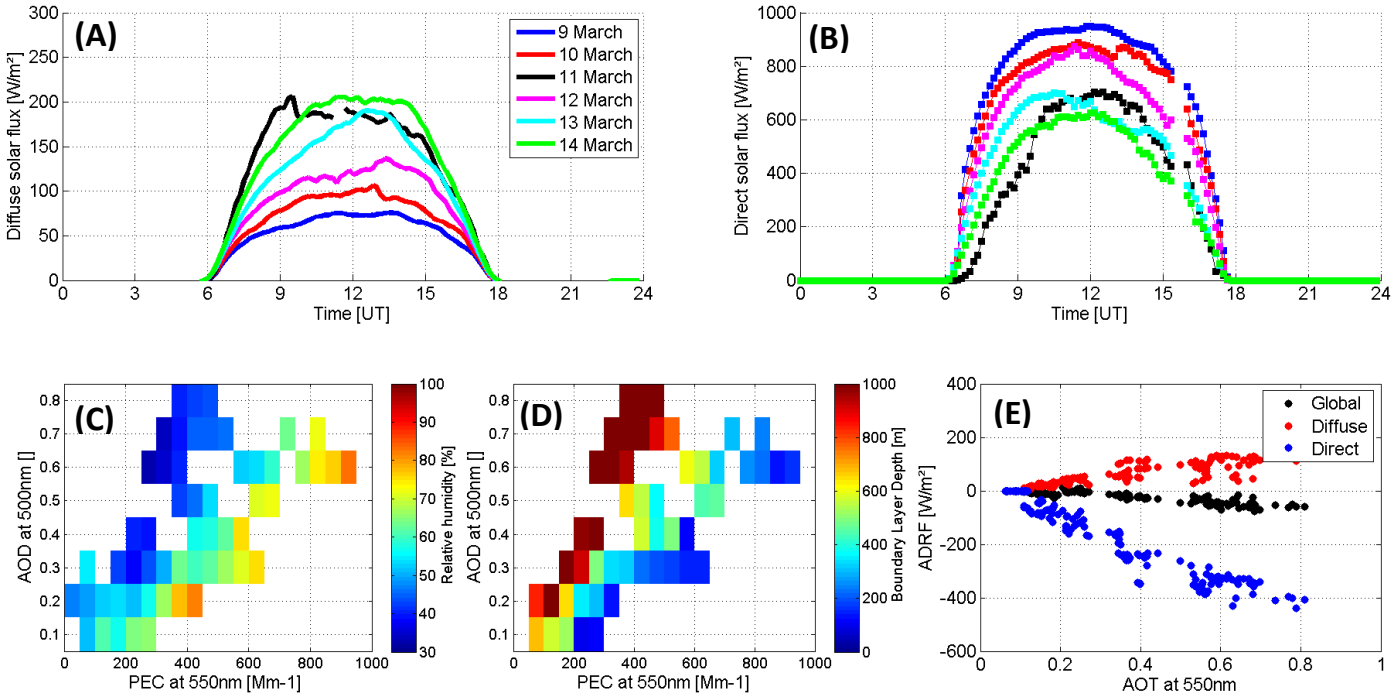

Figure 4. Diurnal cycle of diffuse solar downwelling flux (Fig. 4A) and direct solar downwelling flux (Fig. 4B) between March 9 and March14 2014. Relationship between aerosol optical depth and visible extinction depending on relative humidity (Fig. 4C) and boundary layer depth (Fig. 4D) and between aerosol direct radiative effect and aerosol optical depth for direct, diffuse, and global irradiance (Fig. 4E).

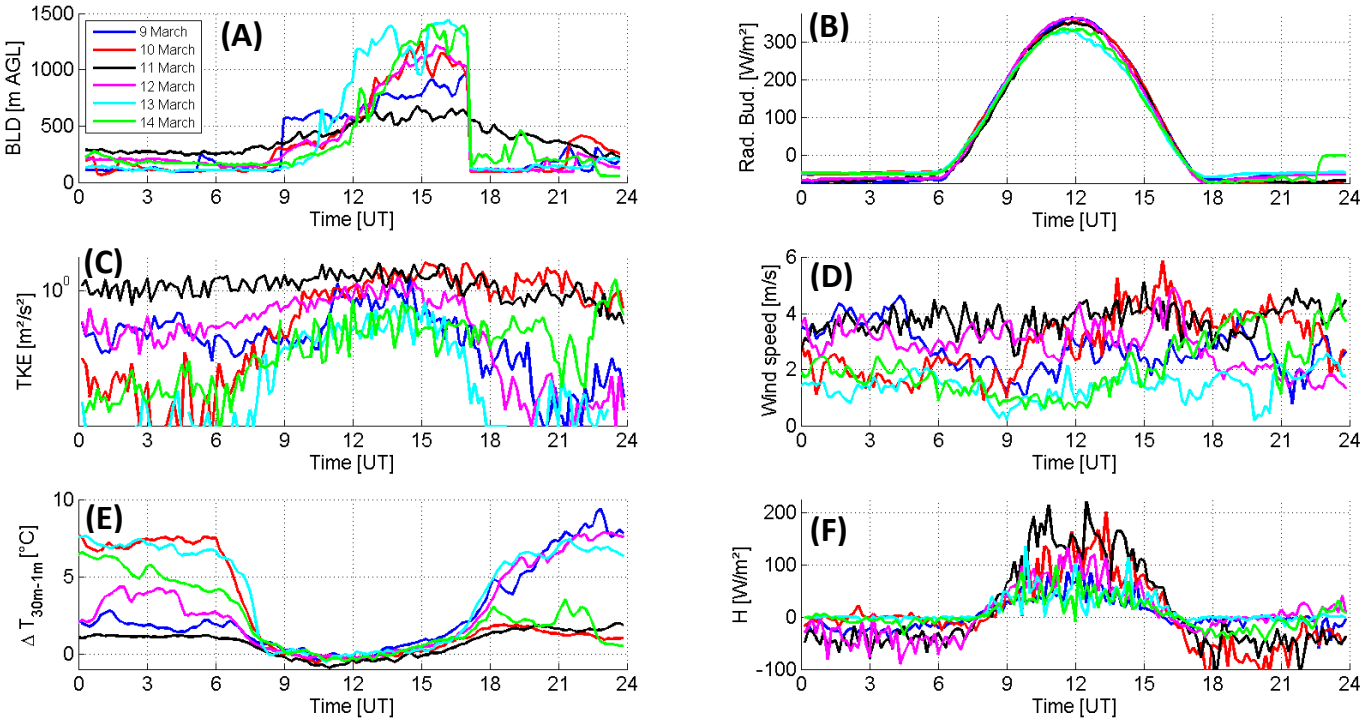

Figure 5. Diurnal cycle of boundary layer depth (Fig. 5A), surface radiative budget (Fig. 5B), turbulent kinetic energy (Fig. 5C), wind speed at 10m agl (Fig. 5D), vertical gradient of temperature (30m-1m,, Fig. 5E), and sensible heat flux at 10m agl (Fig. 5F) between March 9 and March 14 2014.

This event is primarily characterized by a fine particle mass ($PM_{2.5}$) increase from 10 to more than 120 µg m^{-3} and a simultaneous decrease of the horizontal visibility from 40 to 1 km.

The aerosol optical depth (AOD) at 550 nm increased steadily from about 0.06 on March 6 to more than 0.9 five days later.

The mean surface aerosol effect efficiency (effect per unit optical depth) is of about -80 W m^{-2} with a mean aerosol direct radiative effect of -23 W m^{-2}.

A comparative analysis is performed for 4 consecutive days (between March 11 and 14), showing that the $PM_{2.5}$ diurnal cycle can be modulated in time and amplitude by local processes such as the boundary layer depth development (ranging from 100 m to 1350 m), surface relative humidity (100 % to 35 %), thermal structure (10 °C to 16 °C for day/night amplitude), dynamics (wind speed ranging from 4 m s^{-1} to 1.5 m s^{-1}) and turbulence (turbulent kinetic energy reaching 2 m^2 s^{-2}) near the surface and wind shear along the vertical.